

NEQRX: Efficient Quantum Image Encryption with Reduced Circuit Complexity

Rakesh Saini, Bikash K. Behera, Saif Al-Kuwari, and Ahmed Farouk

Abstract—Cryptography plays an important role in ensuring data security and authentication within information processing systems. As the prevalence of digital imagery continues to grow, safeguarding this form of data becomes increasingly crucial. However, existing security protocols, reliant on complex mathematical models, exhibit vulnerabilities in effectively protecting information from both internal and external threats. Moreover, the forthcoming advent of quantum computing poses a significant challenge, as it could decrypt data encrypted by classical. In this paper, we propose an efficient implementation scheme for a quantum image encryption algorithm combining the generalized affine transform and logistic map. We evaluated developed quantum circuits using qiskit and quantum devices to validate the encryption technique. Through comprehensive performance analysis, we have demonstrated the efficiency of the chosen encryption algorithm across various criteria. Furthermore, we introduce a hybrid methodology aimed at mitigating circuit complexity and reducing quantum cost. Leveraging the Espresso algorithm and incorporating an ancilla qubit into the circuitry, we achieve a remarkable 50% reduction in cost while maintaining security and efficiency. Finally, we conducted robustness and security analyses to assess the resilience of our encryption method against diverse noise attacks. The results confirm that our proposed quantum image encryption technique provides a secure solution and offers precise and measurable quantum image processing capabilities.

Index Terms—Novel Enhanced Quantum Representation (NEQR), Generalized Affine Transform (GAT), Logistic Map (LM), Quantum Cost, Complexity Analysis, Noisy Channels, Fidelity.

1 INTRODUCTION

IN the landscape of information science, digital image processing has emerged as a fundamental discipline since its inception in the 1960s [1]. Imaging processing plays an essential role in various fields such as remote sensing, robot vision, pattern recognition, medical field, and many other areas. At its core, digital image processing involves the analysis, transmission, and manipulation of digital imagery, which are represented as two-dimensional arrays or matrices of numbers obtained through sampling and quantization of analog images. The exponential growth in digital image acquisition and sharing and the widespread implementation of machine learning, the Internet of Things, and other technologies have increased the demand for the quality and security of digital images. The quality of digital images depends on factors such as resolution and pixel count, while security concerns revolve around preventing eavesdroppers from accessing sensitive image information. Addressing these tasks requires robust cryptography techniques capable of withstanding sophisticated attacks while also demanding

substantial computational and storage resources. However, existing computing models are not able to meet all these requirements.

Currently, the classical cryptosystems contain data encryption standards (DES), triple-DES, advanced encryption standards, elliptic curve cryptography, and Rivest Shamir Adelman, to name a few. However, while these algorithms are excellent for encryption, they remain vulnerable to the emerging threat posed by quantum computers [2]. Quantum computers have already demonstrated the ability to perform real-time factorization using quantum algorithms, thereby undermining the security of classical cryptographic methods. Moreover, as quantum computers continuously prove their superiority over classical methods, it is pretty close that they will become a reality. Therefore, to ensure the confidentiality and integrity of digital imagery in quantum computing era, it has become necessary to develop encryption techniques using quantum computing principles and achieve post-quantum cryptography [3].

Various proposals have emerged to compute and store the digital image on a quantum computer [4], [5], such as qubit lattice [6], real ket [7], entangle image [8], flexible representation of quantum images (FRQI) [9], multi-channel representation for images (MCQI) [10], novel enhanced quantum representation (NEQR) [11], novel quantum representation of color digital images (NCQI) [12], A Generalized Model of NEQR (GNEQR) [13], normal arbitrary quantum superposition state (NAQSS) [14], and quantum Boolean image processing (QuBoIP) [15]. Of particular interest is the NEQR method, which is very similar to the FRQI except for its approach to encoding the pixel values. NEQR uses eight qubits, hence 2^8 basis states to encode 256 different pixel values, while FRQI uses different polar and azimuthal an-

- Rakesh Saini is with the Qatar Center for Quantum Computing (QC2), College of Science and Engineering, Hamad Bin Khalifa University, Qatar Foundation, Doha, Qatar.
E-mail: rasa68842@hbku.edu.qa
- Bikash K. Behera is with Bikash's Quantum (OPC) Pvt. Ltd., Balindi, Mohanpur 741246, West Bengal, India.
E-mail: bikash@bikashsquantum.com
- Saif Al-Kuwari is with the Qatar Center for Quantum Computing (QC2), College of Science and Engineering, Hamad Bin Khalifa University, Qatar Foundation, Doha, Qatar.
E-mail: smalkuwari@hbku.edu.qa
- Ahmed Farouk is with the Department of Computer Science, Faculty of Computers and Artificial Intelligence, South Valley University, Hurgada, Egypt.
E-mail: ahmed.farouk@sci.svu.edu.eg

gles of a single qubit state. Therefore, NEQR exhibits higher measurement accuracy than FRQI. In addition, quantum encryption algorithms have been developed to transform the original image into a cipher image to secure the information in the image. These encryption procedures include scrambling the pixel positions and/or altering the pixel values using chaos theory or other transformations. These encryption procedures can be categorized into two main types: 1) transforming the image into a frequency domain with random operations [16], [17], [18] and 2) converting the image into an encrypted image using chaos theory [18], [19], [20], [21]. In this study, we focus on the latter type of encryption algorithm by including a logistic map to encrypt the image parameters.

In this paper, we propose an efficient implementation scheme for a novel quantum encryption technique that combines Novel Enhanced Quantum Representation (NEQR) (encoding procedure) [11], generalized affine transform (scrambles the pixel position) [18], and logistic map (changes pixel value using chaos theory) [18]. The quantum circuits and their corresponding algorithms were executed separately on an IBM quantum computer. Then, the Espresso algorithm [22], used in [11], which optimizes circuit complexity has been used with our modified approach. Moreover, the analysis of keyspace, encryption procedure quality, histogram, circuit complexity, and variation in the fidelity of the NEQR circuit is performed under different effectiveness of the noisy channels, including amplitude-damping, phase-damping, bit-flip, phase-flip, bit-phase-flip, and depolarizing.

The contributions of this article can be summarized as follows:

- 1) We propose an efficient scheme for quantum image encryption based on GAT and LM.
- 2) We introduce a hybrid approach to reduce circuit complexity and quantum cost using the Espresso algorithm, which reduced the cost by approximately 50%.

The rest of this paper is organized as follows: Section 2 briefly reviews some preliminaries. Section 3 presents our proposed quantum image encryption algorithm. The evaluation of the keyspace, quality of encryption procedure, histogram, circuit complexity, and robustness test of NEQR circuit in different noisy channels are presented in Section 4. Finally, Section 5 concludes the paper.

2 PRELIMINARIES

2.1 Novel Enhanced Quantum Representation (NEQR)

NEQR, introduced by Zhang et al. [11], offers a novel approach to quantum gray image representation. This model uses $2^n \times 2^n$ gray image parameters as input and encodes them into a quantum circuit. The construction of this circuit involves $2n + 8$ qubits, with 8 qubits designated for storing the gray-scale value $f(Y, X)$ of the pixels, while the remaining $2n$ qubits represent the pixel positions (Y, X) . The resulting state of this quantum circuit encapsulates the entirety of the image. Mathematically, the final state can be expressed as follows:

$$|\psi\rangle = \frac{1}{2^n} \sum_{Y, X=0}^{2^{2n}-1} |f(Y, X)\rangle |YX\rangle, \quad (1)$$

where $|f(Y, X)\rangle$ can be written in the bit sequence as, $\bigotimes_{i=0}^{p-1} |C_{YX}^i\rangle = |c_{YX}^7 c_{YX}^6 \dots c_{YX}^1 c_{YX}^0\rangle$, which represents the encoded gray-scale value of the pixel, and

$$\begin{aligned} |YX\rangle &= |Y\rangle |X\rangle \\ &= |Y_{n-1} Y_{n-2} \dots Y_1 Y_0\rangle |X_{n-1} X_{n-2} \dots X_1 X_0\rangle, \end{aligned}$$

is used to store the corresponding vertical and horizontal coordinate values of the pixels.

Algorithm 1 Algorithm to encode digital images into a quantum circuit using NEQR.

Input: Classical image: $2^n \times 2^n$

Declare the Pixel value: $f(Y, X)$

Declare the vertical and horizontal location of pixels: (Y, X)

Quantum Circuit: QC {initial state $|0\rangle^{2n+8}$ }

Output: Quantum Circuit for given classical image

Initialisation :

- 1: Start by transforming the position and pixel value in binary sequence:

$$(Y, X) \rightarrow |YX\rangle \text{ and } f(Y, X) \rightarrow \bigotimes_{i=0}^7 |C_{YX}^i\rangle$$

- 2: To store these binary numbers in the quantum circuit follow:

(I) The initial state of the circuit: $|0\rangle^{2n+8}$

(II) Apply Hadamard gate on $2n$ -qubits that generate superposition of 2^{2n} states:

$$|0\rangle^8 \otimes (H^{2n} \otimes |0\rangle^{2n}) \rightarrow \frac{1}{2^n} \sum_{Y=0}^{2^n-1} \sum_{X=0}^{2^n-1} |0\rangle^8 \otimes |YX\rangle$$

(III) Define an operation O_{YX} that apply a unitary operation U_{YX} on the pixel value qubits for pixel state $|YX\rangle$ as:

$$O_{YX} = I \otimes \sum_{j=0}^{2^{2n}-1} \sum_{i=0, i,j \neq YX}^{2^{2n}-1} |ij\rangle \langle ij| + U_{YX} \otimes |YX\rangle \langle YX|$$

$$U_{YX} |0\rangle \rightarrow |0 \oplus C_{YX}\rangle$$

(IV) Now, operate O_{YX} on all qubits:

$$\frac{1}{2^n} O_{YX} \left(\sum_{Y=0}^{2^n-1} \sum_{X=0}^{2^n-1} |0\rangle^8 \otimes |YX\rangle \right) \rightarrow$$

$$\frac{1}{2^n} \sum_{Y=0}^{2^n-1} \sum_{X=0}^{2^n-1} (U_{YX} \otimes |0\rangle^8) \otimes |YX\rangle \rightarrow$$

$$\frac{1}{2^n} \sum_{Y=0}^{2^n-1} \sum_{X=0}^{2^n-1} |f(Y, X)\rangle \otimes |YX\rangle \rightarrow |\psi\rangle$$

- 3: **return** QC, $|\psi\rangle$
-

For example, upon performing NEQR on an image of size 2×2 as shown in Fig. 8a, it can be represented by the quantum state:

$$\begin{aligned} |\psi_I\rangle &= \frac{1}{2} (|11111111\rangle |00\rangle + |00000000\rangle |01\rangle \\ &\quad + |11001000\rangle |10\rangle + |01100100\rangle |11\rangle). \end{aligned} \quad (2)$$

Algo. {1} describes the NEQR procedure for encoding digital images into a quantum circuit, and Fig. 1 shows the general quantum circuit for the NEQR method.

2.2 Generalized Affine Transform

GAT, shown in Algo. {2}, scrambles the pixel locations $|YX\rangle$ of the image. Here, X and Y represent the actual horizontal and vertical locations of pixels, respectively [18]. The mathematical representation of GAT, as described in, is given by:

$$\begin{pmatrix} X' \\ Y' \end{pmatrix} = \begin{pmatrix} s & 0 \\ 0 & t \end{pmatrix} \begin{pmatrix} X \\ Y \end{pmatrix} + \begin{pmatrix} P \\ Q \end{pmatrix} \text{ mod } 2^n, \quad (3)$$

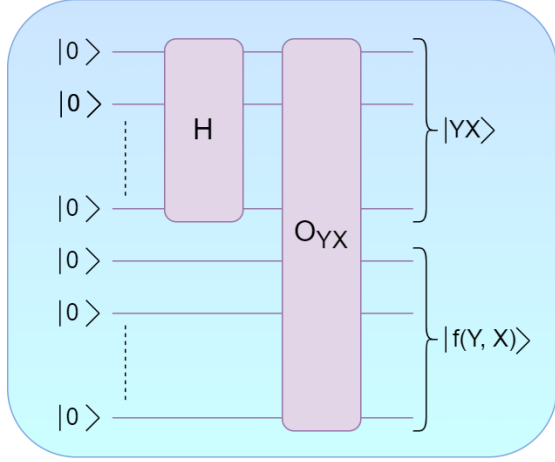


Fig. 1: NEQR procedure circuit using $(2n + 8)$ -qubits. Here, H is the Hadamard gate and O_{YX} is a controlled gate that operate U_{YX} on pixel qubits, when $2n$ -qubits are in the state $|YX\rangle$, to obtain $f(Y, X)$.

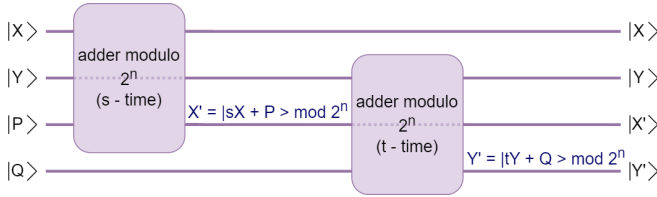


Fig. 2: A quantum circuit for GAT to scramble the original pixel coordinate $|YX\rangle$ into $|Y'X'\rangle$. The dotted qubit line in the circuit represents bypassing the operation.

where X' and Y' represent the scrambled horizontal and vertical locations of pixels, taking the form $(sX + P)$ and $(tY + Q)$, respectively, with modulo 2^n . The parameters s , t , P & Q are for GAT and obey the following conditions:

- P and Q should not be zero. In the circuit implementation, n qubits are allocated for each to store their values.
- s and t should be co-prime with 2^n .

The generalized circuit in Fig. 2 illustrates the operations involved in scrambling the original coordinates $|X\rangle$, $|Y\rangle$ to $|X'\rangle$, $|Y'\rangle$, as calculated in Equation (3). The inverse operation of GAT, depicted in Algo. 4, is utilized to recover the original pixel coordinates from the scrambled ones. Mathematically, this inverse operation can be expressed as:

$$\begin{pmatrix} X \\ Y \end{pmatrix} = \begin{pmatrix} s^{-1} & 0 \\ 0 & t^{-1} \end{pmatrix} \begin{pmatrix} X' - P \\ Y' - Q \end{pmatrix} \text{ mod } 2^n. \quad (4)$$

This equation gives the original coordinates of the pixel $X = s^{-1}(X' - P) \text{ mod } 2^n$ and $Y = t^{-1}(Y' - Q) \text{ mod } 2^n$. Here, s^{-1} and t^{-1} are the modular multiplicative inverse [23] of s and t , respectively, and can be calculated as follows:

$$\begin{aligned} 1 &= ss^{-1} \text{ mod } 2^n, \\ 1 &= tt^{-1} \text{ mod } 2^n. \end{aligned} \quad (5)$$

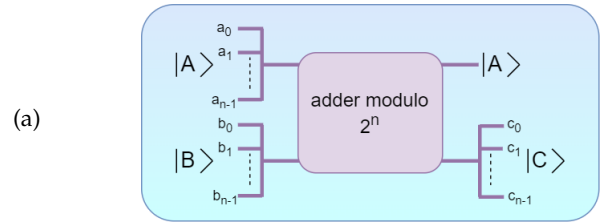
The generalized circuit in Fig. 4 shows the operations performed to recover the original coordinates $|X\rangle$, $|Y\rangle$ from $|X'\rangle$, $|Y'\rangle$ as calculated in Eq. (4).

Algorithm 2 Algorithm to encrypt pixel positions by using GAT.

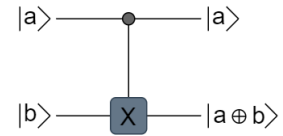
Input: Declare the size of the image: $2^n \times 2^n$
 Declare the GAT parameters: P ,
 Q , s and t
 Declare the horizontal and vertical location
 of pixels: X, Y

Output: Image of scrambled pixel location

Initialisation :
 1: $i, j \leftarrow 1$
 2: **while** $i \leq s$ **do**
 3: $X' = (iX + P) \text{ mod } 2^n$
 4: $i \leftarrow i + 1$
 5: **end while**
 6: **while** $j \leq t$ **do**
 7: $Y' = (jY + Q) \text{ mod } 2^n$
 8: $j \leftarrow j + 1$
 9: **end while**
 10: **return** X', Y'



(a)



(b)

Fig. 3: (a) Adder modulo circuit: with output $|C\rangle = |A\rangle \oplus |B\rangle \text{ mod } 2^n$. (b) Quantum CNOT gate: gives output as $a \oplus b \text{ mod } 2$.

2.3 Adder modulo 2^n

The adder modulo 2^n is designed to sum two binary numbers, each represented by n -bits, ensuring that the resultant binary number maintains the same number of bits. This is achieved by ignoring the last carry bit. A generalized quantum circuit for the adder modulo 2^n is given in [24]. A general black-box representation of this circuit for $2n$ -bits input is shown in Fig. 3a. For $n = 1$, the adder modulo 2^n circuit simplifies to the quantum CNOT gate, shown in Fig. 3b.

2.4 Logistic Map

LM is used to iteratively map the value of the previous step to the next step [21], using the following dynamic equation:

$$L_{\eta+1} = \delta L_{\eta}(1 - L_{\eta}), \quad (6)$$

where $\eta = 0, 1, 2, \dots, 2^{2n} - 1$. Here, $L_0 \in (0, 1)$ denotes the initial value of LM, δ represents the growth rate, and 2^{2n} signifies the total number of pixels.

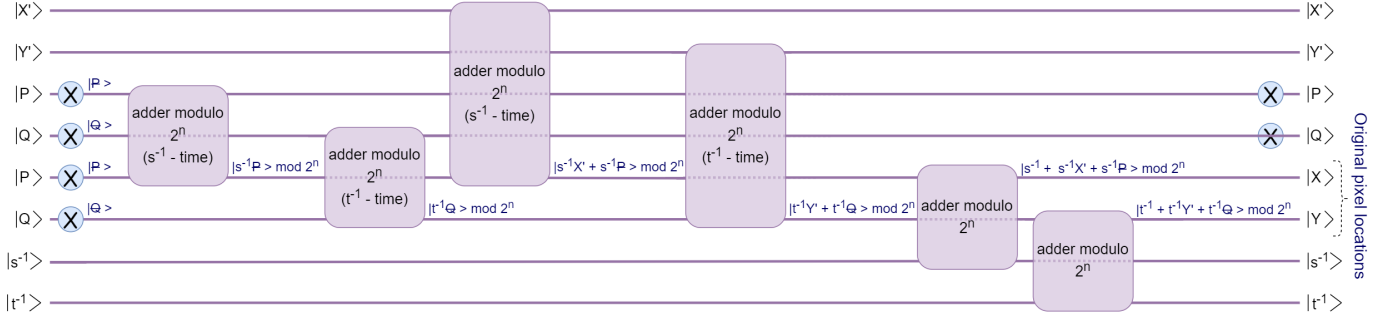


Fig. 4: Quantum circuit represents a General decryption procedure for GAT to obtain the real pixel coordinate $|YX\rangle$ from $|Y'X'\rangle$. The dotted qubit line refers to avoiding the applied operation.

This dynamic equation exhibits chaotic behavior for $3.85 \leq \delta \leq 4$, which means that with this growth rate, Eq. (6) generates pseudo-random strings of 0's and 1's.

3 PROPOSED ALGORITHM

3.1 NEQR Circuit

In Fig. 10a, where $n = 1$, a quantum circuit of $2 + 8$ -qubits is initialized in all 0's state. The first 2-qubits store the pixel coordinates, while the rest represent pixel values. The encoding procedure of the image parameters in a quantum circuit, as outlined in Algorithm {1}, is as follows:

- 1) The image, shown in Fig. 8a, has 4-pixels with different positions and values. To process all pixel positions, the Hadamard gates on the first 2-qubits are employed that generate a superposition of four equally probable states $(|00\rangle, |01\rangle, |10\rangle, \text{ and } |11\rangle)$.
- 2) Toffoli gates are then applied, using coordinate qubits as control and the remaining qubits as targets. These Toffoli gates transform the pixel value qubits from state $\bigotimes_{i=0}^7 |0^i\rangle$ to state $\bigotimes_{i=0}^7 |C_{YX}^i\rangle$, corresponding to each pixel $|YX\rangle$.

The conversion of the state of the quantum circuit is as follows:

$$\begin{aligned} |000000000\rangle &\xrightarrow[\text{first 2-qubits}]{\text{apply H-gate on}} |00000000\rangle |++\rangle \\ &\xrightarrow[\text{on rest qubits}]{\text{apply Toffoli gates}} |\psi_I\rangle. \end{aligned} \quad (7)$$

The resultant quantum circuit for this whole procedure is shown in Fig. 10a, featuring 14 Toffoli gates. However, before executing on real superconducting devices, the circuit must be transpiled to the device's basis gates, which can exponentially increase circuit size and depth, impacting execution efficiency and fidelity.

To overcome this problem, the image compression in [11] is used. This procedure handles the control bit strings of the pixel values using the Espresso algorithm [22] so that a similar task can be performed with a lower control bit string, as shown in Fig. 5. As a result, the circuit complexity is reduced. In this compression procedure, an extra step has been added to reduce the circuit complexity further. This step uses an ancillary qubit to store the information of the Toffoli gates, which are then used as control and target the desired qubits one by one using C-NOT gates. The same task can be implemented using a few Toffoli gates, C-NOT gates, and one ancillary qubit, see Fig. 10c. This step is used when

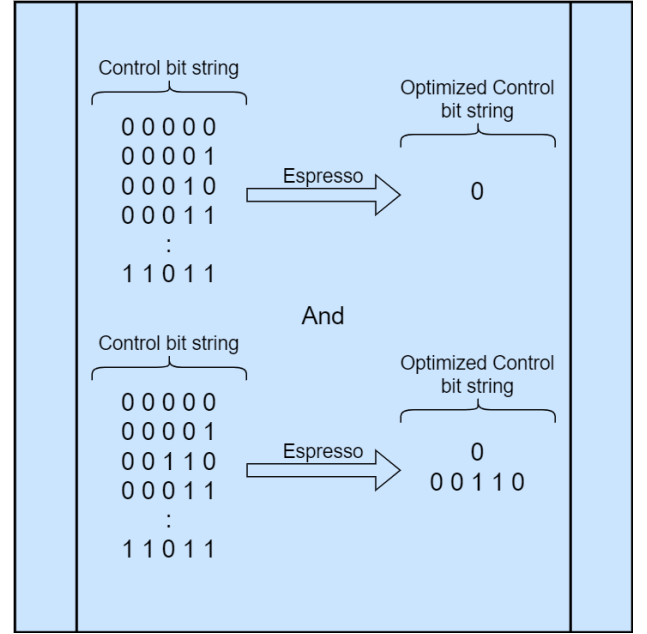


Fig. 5: An example to demonstrate the optimization of control bit strings using the Espresso algorithm. The original control bits strings on the left and the optimized control bit strings on the right can perform the same operation on the i^{th} target qubit.

the number of Toffoli gates with the same control bit string is still high after using the image compression procedure [11]. Fig. 10b and Fig. 10d illustrate a comparison.

3.2 Encryption procedure

The encryption procedure utilizes a combination of LM and GAT to transform the original image into an encrypted form.

3.2.1 logistic map (Diffusion stage)

The diffusion stage is applied to the value of the pixel and is controlled by the corresponding pixel coordinates. This stage utilizes chaos theory as described in Section 2.4, resulting in a chaotic image. The quantities required to operate LM in a quantum circuit are calculated according to Algo. {3}. The operations of LM in a quantum circuit are as follows:

- 1) Pick the output lists J, T of Algo. {3}.

- 2) Transform each J_{YX} and T_{YX} form J and T to a binary sequence as:

$$|J_{YX}\rangle = \otimes_{i=0}^{p-1} |J_{YX}^i\rangle, \quad |T_{YX}\rangle = \otimes_{i=0}^{p-1} |T_{YX}^i\rangle. \quad (8)$$

- 3) Defining quantum operations D_{YX} and E_{YX} to manipulate pixel values based on J_{YX} and T_{YX} as:

$$D_{YX} |C_{YX}^i\rangle \rightarrow |C_{YX}^i \oplus J_{YX}^i\rangle, \\ E_{YX} |C_{YX}^i \oplus J_{YX}^i\rangle \rightarrow |C_{YX}^i \oplus J_{YX}^i \oplus T_{YX}^i\rangle.$$

- 4) Define functions that apply D_{YX} and E_{YX} ,

$$\phi_{YX}^1 = I \otimes \frac{1}{2^n} \sum_{j=0}^{2^n-1} \sum_{i=0, j \neq YX}^{2^n-1} |ji\rangle \langle ji| + D_{YX} \\ \otimes |YX\rangle \langle YX|, \\ \phi_{YX}^2 = I \otimes \frac{1}{2^n} \sum_{j=0}^{2^n-1} \sum_{i=0, j \neq YX}^{2^n-1} |ji\rangle \langle ji| + E_{YX} \\ \otimes |YX\rangle \langle YX|.$$

- 5) Apply ϕ_{YX}^1 and ϕ_{YX}^2 on the quantum state $|\psi_I\rangle$ as:

$$|\psi_L\rangle = \phi_{YX}^2 \phi_{YX}^1 |\psi_I\rangle \\ = \frac{1}{2^n} \sum_{Y,X=0}^{2^{2n}-1} (E_{YX} D_{YX} \bigotimes_{i=0}^{p-1} |C_{YX}^i\rangle) |YX\rangle \\ = \frac{1}{2^n} \sum_{Y,X=0}^{2^{2n}-1} \bigotimes_{i=0}^{p-1} |C_{YX}^i \oplus J_{YX}^i \oplus T_{YX}^i\rangle |YX\rangle.$$

3.2.2 Generalized Affine Transform (Permutation stage)

GAT, represented by the operator A , operates only on the pixel positions of the quantum state of the image $|\psi_L\rangle$. The operation is as follows:

$$|\psi_{AL}\rangle = A |\psi_L\rangle = \frac{1}{2^n} \sum_{Y=0}^{2^n-1} \sum_{X=0}^{2^n-1} |f'(Y, X)\rangle A |YX\rangle \\ = \frac{1}{2^n} \sum_{Y=0}^{2^n-1} \sum_{X=0}^{2^n-1} |f'(Y, X)\rangle |Y'X'\rangle,$$

where A scrambles the horizontal and vertical positions of the pixels as $A|X\rangle = |X'\rangle$ and $A|Y\rangle = |Y'\rangle$, respectively. This transformation is described in Algo. {2} and the output of this algorithm $|X'\rangle$ and $|Y'\rangle$ are given by:

$$|X'\rangle = |sX + P\rangle \bmod 2^n, \\ |Y'\rangle = |tY + Q\rangle \bmod 2^n.$$

According to the quantum version of GAT to scramble pixel positions, a general quantum circuit given in Fig. 2 is designed. This quantum circuit performs the adder modulo 2^n operation, s and t times to transform the states $|X\rangle \rightarrow |X'\rangle$ and $|Y\rangle \rightarrow |Y'\rangle$, respectively, as shown in Fig. 2. The algebra of quantum circuit is as follows:

$$|X, P\rangle \xrightarrow[s \text{ - times}]{\text{adder modulo } 2^n} |X, (sX + P) \bmod 2^n\rangle, \\ |Y, Q\rangle \xrightarrow[t \text{ - times}]{\text{adder modulo } 2^n} |Y, (tY + Q) \bmod 2^n\rangle.$$

3.3 Decryption procedure

Decryption involves reversing GAT and LM procedures.

Algorithm 3 Algorithm to encrypt pixel values by using LM.

Input: Declare the size of the image: $2^n \times 2^n$
Declare the LM parameters: δ, L_0

Output: $J_{YX}, T_{YX} \{YX = \eta\}$

Initialisation :

```

1:  $J, T = [ ]$ 
2: for all  $\eta$  in range( $2^{2n} - 1$ ) do
3:    $L_{\eta+1} = \delta L_{\eta}(1 - L_{\eta})$ 
4:    $J_{YX} = \text{round}(\text{mod}(L_{\eta} \times 2^8, 2^8))$ 
5:    $J.append(J_{YX})$ 
6: end for
7: for all  $\eta$  in range( $2^{2n} - 1$ ) do
8:    $T_{YX} = J_{2^{2n}-1-YX}$ 
9:    $T.append(T_{YX})$ 
10: end for
11: return  $J, T$ 

```

3.3.1 Inverse Generalized Affine Transform

The inverse GAT retrieves the original horizontal and vertical pixel coordinates of the image. Let A^{-1} be the inverse GAT operation:

$$|\psi_L\rangle = A^{-1} |\psi_{AL}\rangle \\ = \frac{1}{2^n} \sum_{Y,X=0}^{2^{2n}-1} |f'(Y, X)\rangle A^{-1} |Y'X'\rangle \\ = \frac{1}{2^n} \sum_{Y,X=0}^{2^{2n}-1} |f'(Y, X)\rangle |YX\rangle.$$

According to Theorem 3 in [16], the negative adder modulo 2^n in the Eq. (4) can be realized as:

$$(x - y) \bmod 2^n = (x + (\bar{y} + 1)) \bmod 2^n,$$

where $\bar{y} = \bar{y}_{n-1}\bar{y}_{n-2}\dots\bar{y}_0 = 1 - y_i$ with $i = n - 1, n - 2, \dots, 0$. Thus, $X = s^{-1}(X' - P) \bmod 2^n$ is converted to $X = s^{-1}(X' + (\bar{P} + 1))$ and similarly for Y . The circuit in Fig. 4 takes $2s^{-1} + 3$ steps to obtain the original pixel position $|X\rangle$ and $2t^{-1} + 3$ for $|Y\rangle$. Refer to Algo. {4} for a step-by-step explanation of the inverse GAT procedure.

3.3.2 logistic map

The inverse LM procedure is very simple with the output of Algo. {3}. This procedure operates the same functions ϕ_{YX}^1 and ϕ_{YX}^2 used in the encryption procedure (see Fig. 7) as:

$$|\psi\rangle = \phi_{YX}^1 \phi_{YX}^2 |\psi_L\rangle \\ = \phi_{YX}^1 \phi_{YX}^2 \phi_{YX}^2 \phi_{YX}^1 |\psi\rangle \\ = \frac{1}{2^n} \sum_{Y,X=0}^{2^{2n}-1} (D_{YX} E_{YX} E_{YX} D_{YX} \bigotimes_{i=0}^{p-1} |C_{YX}^i\rangle) |YX\rangle \\ = \frac{1}{2^n} \sum_{Y,X=0}^{2^{2n}-1} \bigotimes_{i=0}^{p-1} |C_{YX}^i\rangle |YX\rangle. \quad (9)$$

4 EVALUATION

Image reconstruction is performed using the pixel values and pixel positions obtained after the simulation of the quantum circuits (constructed according to Fig. 1) in the

Algorithm 4 Algorithm to decrypt the pixel values using GAT.

Input: Declare the GAT parameters: P, Q, s and t
 Declare the scrambled image pixel location:
 X', Y'
 Quantum Circuit for the location of pixels: QC_1
 (QC_1 has $2n$ qubits)
 Quantum Circuit to store P and Q : QC_2
 (QC_2 has $2n$ -qubits, n to store P and rest for Q)
 GAT operator: A (Adder modulo 2^n)

Output: Original image
Initialisation :
 1: Apply A on \overline{P} {as control} to \overline{P} {as target}
 2: **for all** i in range($1, 2s^{-1} + 4$) **do**
 3: **for all** $1 \leq i \leq s^{-1}$ **do**
 4: $\overline{P} \leftarrow (i\overline{P}) \bmod 2^n$
 5: **end for**
 6: **for** $i = s^{-1} + 1$ **do**
 7: Replace \overline{P} {control} to X' {control}
 8: **end for**
 9: **for all** $s^{-1} + 2 \leq i \leq 2s^{-1} + 1$ **do**
 10: $\overline{P} \leftarrow (iX' + s^{-1}\overline{P}) \bmod 2^n$
 11: **end for**
 12: **for** $i = 2s^{-1} + 2$ **do**
 13: Replace X' {control} to s^{-1} {control}
 14: **end for**
 15: **for** $i = 2s^{-1} + 3$ **do**
 16: $\overline{P} \leftarrow (s^{-1} + s^{-1}X' + s^{-1}\overline{P}) \bmod 2^n$
 17: **end for**
 18: **end for**
 19: **do** $\overline{P} \leftarrow \overline{Q}, s^{-1} \leftarrow t^{-1}, X' \leftarrow Y'$ repeat from 1 to 18 **for**
 Y
 20: **return** $\overline{P} = X$ and $\overline{Q} = Y$

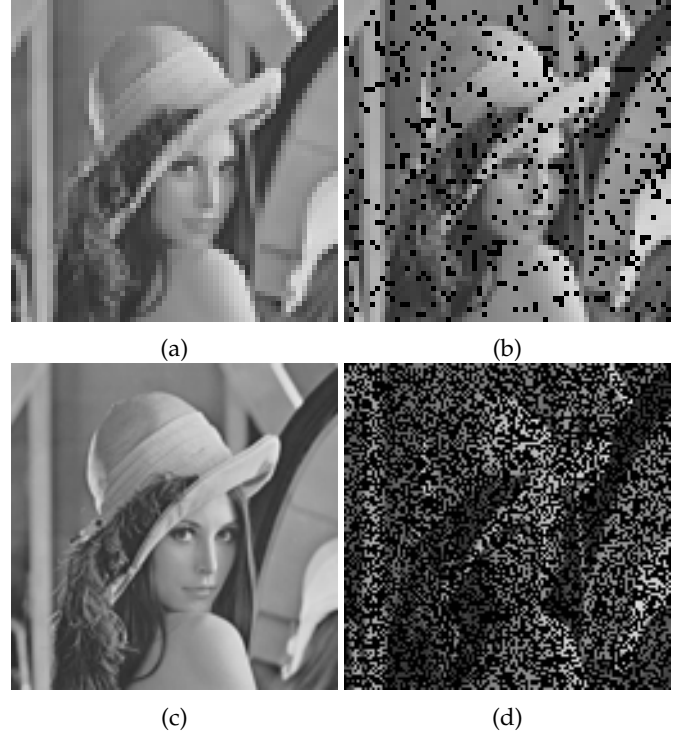


Fig. 6: The figure shows two original and two simulated images as per Fig.1: (a) The original Lena image of size 64×64 . (b) The simulated result of the Lena image of size 64×64 with shots = 8192. (c) The original Lena image of size 128×128 . (d) The simulated result of the Lena image of size 128×128 with shots = 8192. Increasing the number of shots/measurements enhances image quality by providing more probable states.

Qiskit Qasm simulator, which resembles a real perfect quantum computer [25]. The results are presented in Fig. 6.

4.1 Correlation Coefficient Analysis

The correlation coefficient r of two images is the analysis of how much these images are correlated to each other. The mathematical formula for the correlation coefficient is:

$$r = \frac{\sum(x_i - x_m)(y_i - y_m)}{\sqrt{\sum(x_i - x_m)^2 \sum(y_i - y_m)^2}},$$

where x_i is the i_{th} pixel intensity in the original image, y_i is the i_{th} pixel intensity in the encrypted image, x_m & y_m are the mean pixels intensity of the original and encrypted image, respectively.

One can decide on the correlation based on the value of r such that,

- $r = 1$: images are identical
- $r = 0$: images are uncorrelated
- $r = -1$: one image is the negative of the other

After using the values of each pixel intensity from Table I, the value of the correlation coefficient r turns out to be -1, which means that the encrypted image in Fig. 8c is the negative image of the original image in Fig. 8a.

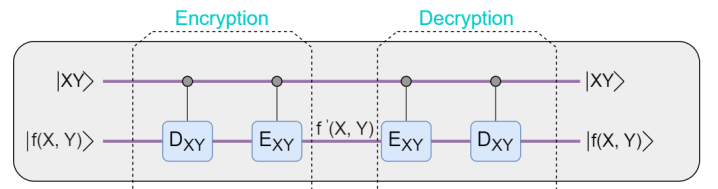


Fig. 7: LM for encryption and decryption of pixel value guided by horizontal X and vertical Y position of pixels.

pixel position	plain image	encrypted image
$ 00\rangle$	255	213
$ 01\rangle$	0	37
$ 10\rangle$	200	237
$ 11\rangle$	100	78
mean value	139	141

TABLE I: Table shows the pixel intensity of plain and encrypted images corresponding to their position in the image.

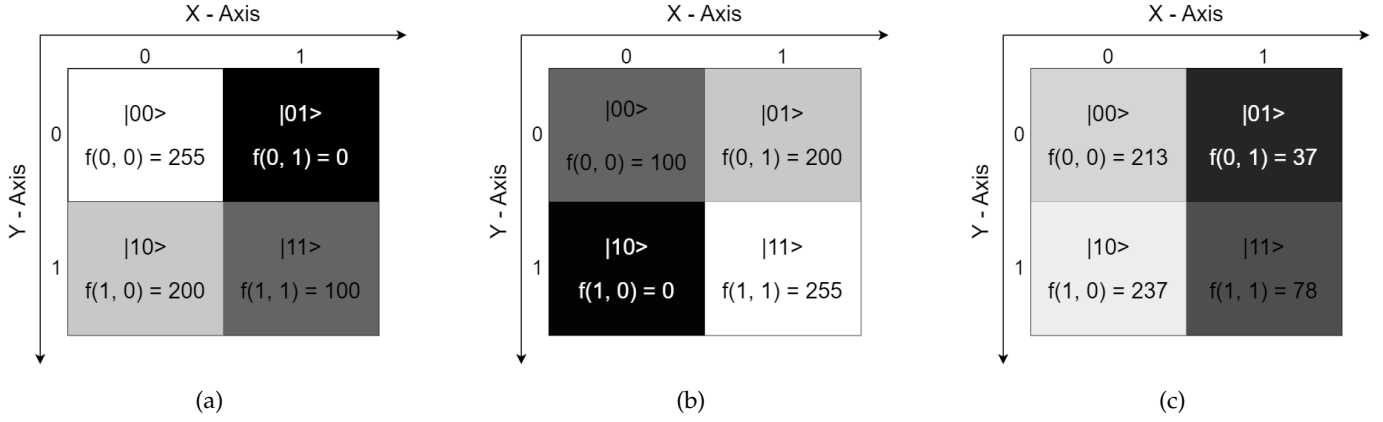


Fig. 8: The figure shows three different images: (a) Original image for Eq. (2). (b) encrypted image using GAT. (c) Encrypted image using both GAT and LM. Here, the generalized affine encryption with $P, Q, s, t = 1$ and LM encryption with $L_0 = 0.5557924316949603$ and $\delta = 3.9816188727791215$.

is presented.

image	$NPCR$ (in %)	$UACI$ (in %)
encrypted image (same parameter)	25	0.098
encrypted image (different parameter)	100	28.04

TABLE II: Table shows the values of $NPCR$ and $UACI$. In the first row, for the images in Fig. 8c and in Fig. 9a. In second row, for the images in Fig. 8c and in Fig. 9c.

4.2 Encryption Analysis

The effectiveness of the encryption procedure depends on the keyspace, key sensitivity, and its ability to generate different encrypted images for minor changes in the original image.

4.2.1 keyspace

keyspace is the storage space that consists of all the possible combinations of keys for an encrypted system such that one of them can decrypt the system perfectly. The keyspace rises with the number of bits (n), and can be represented as:

$$keyspace(KS) \propto 2^n.$$

For GAT, n_P, n_Q, n_s, n_t -qubit have been used to store the parameters $P, Q, s,$ and t , respectively. Hence, the keyspace for GAT is $KS_A = 2^{n_P+n_Q+n_s+n_t}$. For LM, n_{L_0} and n_δ -qubit for L_0 and δ , have been used. Hence, the keyspace is $KS_L = 2^{n_{L_0}+n_\delta}$. In total, the keyspace is $KS_T = KS_A + KS_L$.

To encrypt the image, one should select the encryption parameters (P, Q, s, t, L_0, δ) so that a brute-force attack (trying all possible combinations of the key) cannot break the encryption in the feasible amount of time. However, as discussed in [18], L_0 and δ are infinite decimals, so the keyspace becomes infinite. Therefore, the encrypted image resists brute-force attacks.

4.2.2 Differential Analysis

Two differential analysis experiments were conducted to assess the sensitivity of the encryption procedure to changes

in the encryption key and the original image. In the first experiment, the value of the pixel at position (0, 0) is changed from 255 to 254, producing the encrypted image shown in Fig. 9a. Fig. 9b shows the differential image between the image of the original encrypted image 8c and the encrypted image after a change in the pixel value 9a. The difference can be measured by the number of pixels change rate ($NPCR$) and unified average changing intensity ($UACI$) as follows:

$$NPCR = \frac{1}{W \times H} \left[\sum_{i,j} D(i,j) \right] \times 100\%,$$

$$UACI = \frac{1}{W \times H} \left[\frac{\sum_{i,j} |C(i,j) - C'(i,j)|}{255} \right] \times 100\%,$$

where W and H represent the width and height of the image, respectively. $D(i, j)$ is determine as,

$$D(i, j) = \begin{cases} 1 & \text{for } C(i, j) = C'(i, j), \\ 0 & \text{for } C(i, j) \neq C'(i, j), \end{cases}$$

where $C(i, j)$ and $C'(i, j)$ are the pixel values at the coordinate (i, j) of the images in Fig. 8c and in Fig. 9a, respectively.

The second experiment consists of altering the value of the key parameter L_0 from 0.5557924316949603 to 0.6 while keeping all the other keys unchanged. The resulting encrypted image is depicted in Fig. 9c. Then, the difference between the modified and original encrypted images is calculated. Finally, a differential image, illustrated in Fig. 9d, is constructed that demonstrates that the new encrypted image is entirely different from the previous encrypted image 8c. Thus, even a slight alteration in L_0 leads to generating a completely different image, highlighting the sensitivity of the encryption procedure to the key parameters.

The $NPCR$ s and $UACI$ s are listed in Table II, which shows that our encryption method is not too sensitive to plain text, while it is highly sensitive to encryption keys (a slight change in encryption key results in a completely different encrypted image).

4.2.3 Pear-signal-to-noise-ratio Analysis

The peak-signal-to-noise-ratio ($PSNR$) is a popular metric to measure the fidelity between two images. Here, the

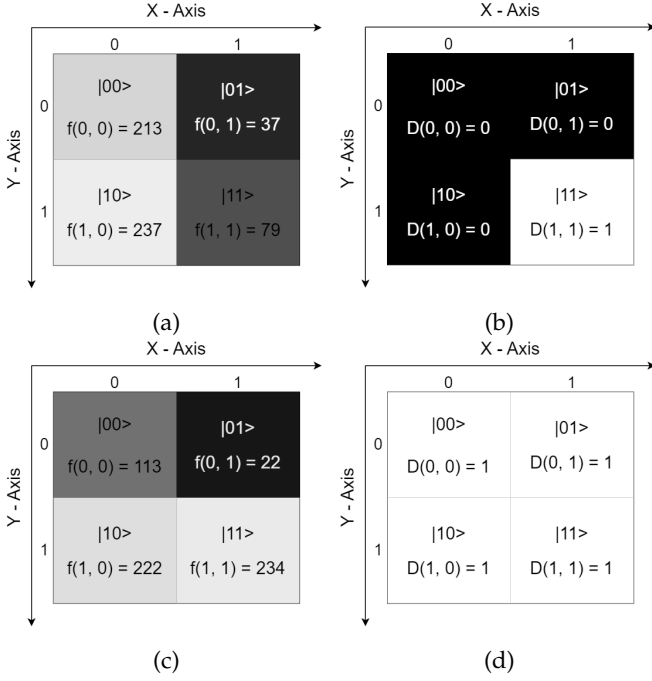


Fig. 9: The figure shows two encrypted and two differential images: (a) is the encrypted image of Fig. 8a with a change in the pixel value of the pixel at position (0, 0) from 255 to 254. (b) is the differential image of Fig. 9a and Fig. 8c. (c) is the encrypted image of Fig. 8a with change in key L_0 from 0.5557924316949603 to 0.6, while the other keys are intact. (d) is a differential image of Fig. 9c and Fig. 8c.

original image from Fig. 8a and the encrypted image from Fig. 8c are considered [26], [27], [28]. The higher the $PSNR$, the lower the quality of encryption. The $PSNR$ is defined as follows:

$$PSNR = 20 \log_{10} \left(\frac{MAX_I}{\sqrt{MSE}} \right), \quad (10)$$

where MAX_I is the maximum possible pixel value of original image and MSE is the mean squared error, which for two $m \times n$ monochromatic images is defined as [29],

$$MSE = \frac{1}{mn} \sum_{i=0}^{m-1} \sum_{j=0}^{n-1} [I(i, j) - K(i, j)], \quad (11)$$

where the $I(i, j)$ and $K(i, j)$ represents the pixel value of i^{th} row & j^{th} column of the original and encrypted image, respectively. The higher the value of MSE , the better the encryption procedure. The error is the quantity degradation by which the pixel value of the original image changes to form the encrypted image. The value of MSE turns out to be 25 based on the images from Fig. 8a and Fig. 8c, and the MAX_I is 255, so the $PSNR$ value is 34.1514 dB, which is acceptable because for 8-bit data the $PSNR$ value varies from 30 db to 50 db [29], [30].

4.3 Histogram Analysis

The analysis of the histogram includes image reconstruction using the information obtained from the histogram. In the histogram, the order of the state is represented as

$|q_9 \dots q_2 q_1 q_0\rangle \rightarrow |C_0 \dots C_7 Y X\rangle$. By converting this binary state to decimal format, both the pixel location (YX) and its corresponding pixel value ($f(Y, X)$) can be re-calculated.

4.4 Complexity analysis

To assess the complexity of the quantum circuit, the following two key metrics are used: 1) quantum cost: the number of elementary quantum gates used in the quantum circuit and 2) time complexity: It denotes the depth or the number of time steps in the execution of the quantum circuit (where the execution of all basis operations in one step is taken as 1 unit).

4.4.1 Quantum cost

In our case, the part of the circuit that affects the quantum cost is the encoding of the pixel values according to the positions of the pixels because this part includes several \mathbb{C}^{2n} (NOT gates). These gates are decomposed into $2(2n - 1)$ Toffoli gates and a c-NOT gate with $2n - 1$ ancillary qubit, where \mathbb{C}^{2n} represents the $2n$ control qubits. In total, the decomposition of \mathbb{C}^{2n} NOT gate into basis single and two-qubit gates will increase the cost enormously.

This increase in cost can be minimized with the help of the Espresso algorithm. The algorithm takes the control qubits information and returns a circuit that performs the same control task but with fewer control qubits. For example, the NEQR circuit in Fig. 10a, which has 14 Toffoli gates is optimized and reduced to the circuit in Fig. 10b, which has only 8 Toffoli gates by applying the Espresso algorithm. The quantum cost for the quantum circuit shown in Fig. 10a is 234, which reduces to 154 after the application of the Espresso algorithm. To further optimize the quantum cost, the technique demonstrated in Fig. 10c has been deployed, resulting in the conversion of our circuit to Fig. 10d with a quantum cost of 91. This reduction in quantum cost is considerable; as with the Espresso algorithm and the presented technique, the total cost of the NEQR quantum circuit in Fig. 10a decreases to 38.89%, compared to 65.81% without employing the technique depicted in Fig. 10c.

4.4.2 Time complexity

As discussed in [11], the time complexity of the NEQR circuit is not greater than $\mathcal{O}(qn2^{2n})$. Similarly, in [18], it was shown that the time complexity of the encryption procedure is $\mathcal{O}(n)$, which is the same for the decryption procedure.

The quantitative analysis of the time complexity of the NEQR circuit, after encryption and decryption, is presented in Table III. Additionally, after including the technique shown in Fig. 10c, the time complexity is optimized significantly with the expense of adding one ancillary qubit. From Table III, it is evident that the time complexity is reduced to 35.38%, a substantial improvement compared to 63.26% without employing the technique shown in Fig. 10c.

4.5 Noise Analysis

Current small-scale quantum computers are inherently noisy, necessitating consideration of noise effects for realistic simulations. In this section, we adopt six different types of noisy environments, namely amplitude-damping, phase-damping, bit-flip, phase-flip, bit-phase-flip, and depolarizing. These noisy channels are characterized by Kraus operators [31]. To observe the effect of a particular noise on

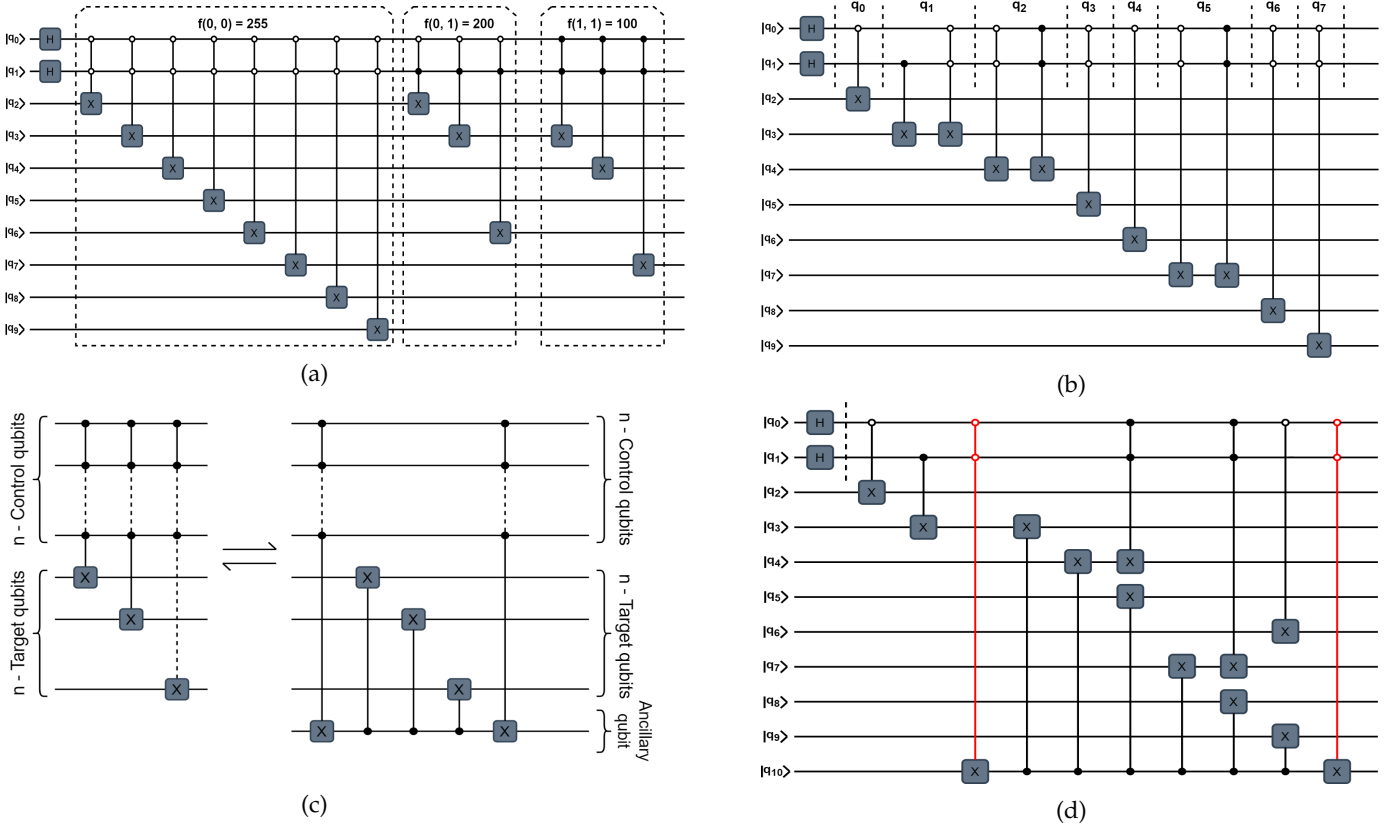


Fig. 10: (a) Quantum circuit for classical image shown in Fig. 8a, according to the NEQR quantum model. Note that the position coordinates of the pixel are encoded into the circuit as $|YX\rangle \rightarrow |q_1q_0\rangle$ and the pixel values as $|C_{YX}^0 C_{YX}^1 \dots C_{YX}^7\rangle \rightarrow |q^9 q^8 \dots q^2\rangle$. (b) The quantum circuit represents the circuit shown in Fig. 10a after the reduction in the controlled information for the pixel values using the Espresso algorithm. (c) The figure shows the quantum circuit to reduce the number of Toffoli gates with the help of one ancillary qubit. (d) The figure shows the quantum circuit after the application of the Espresso algorithm and the technique presented in Fig.10c. The Toffoli gate represented by red is the one whose information is saved in the ancillary qubit.

	Circuit	Quantum cost	Time complexity
Normal	NEQR	234	147
	Encryption	666	513
	Decryption	1126	887
with Espresso	NEQR	154	93
	Encryption	374	247
	Decryption	597	403
including presented technique	NEQR	91	52
	Encryption	216	134
	Decryption	342	215

TABLE III: Computational Complexities of the NEQR, NEQR with encryption, and NEQR with encryption and decryption quantum circuits for image 8a. The calculation is done using the qiskit transpiler with optimization level = 3 and basis gate set = [cx, id, rz, sx, x], which is the most common basis gate set for IBM's quantum hardware. In the 2nd row the values are calculated without any circuit compression methods. In 3rd row the values are calculated with the Espresso algorithm compression method and in the 4th row the values are calculated with the Espresso algorithm & with the presented compression method shown in Fig. 10c. The unit of quantum cost is the number of gates and time complexity is the time steps taken to operate all the possible quantum gates that can be simulated simultaneously.

a circuit, the corresponding Kraus operator should affect each qubit of the circuit or the qubits that will have a noisy impact. This noise transforms the pure quantum state ($|\psi\rangle$) to a mixed state, whose properties are best described by the density matrix ($\rho = |\psi\rangle\langle\psi|$). The effect of noise on the pure state ψ is formulated as:

$$\epsilon^r(\rho) = \sum_m (\otimes_{i=0}^n K_m^{r q_i}) \rho (\otimes_{i=0}^n K_m^{r q_i \dagger}),$$

where K_m represents the Kraus operators, r signifies the type of noisy environment, q_i denotes the qubit on which noise acts, and n is the number of qubits. The effect of noise on the real quantum state $|\psi\rangle$ can be quantified by calculating the fidelity. Fidelity is a measure of the closeness between two quantum states and is given by:

$$F(\rho, \epsilon(\rho)) = \left[\text{Tr} \sqrt{\sqrt{\rho} \epsilon(\rho) \sqrt{\rho}} \right]^2, \quad (12)$$

where $\rho = |\psi\rangle\langle\psi|$ is the pure state, $\epsilon(\rho)$ is the noisy state, and $F(\rho, \epsilon(\rho)) \in [0, 1]$, where 1 means both states are identical, and 0 means the states are entirely different.

Note that all noisy simulations are done only for the NEQR circuit (excluding the rest of the circuit) because of

resource limitations. This is due to the dimension of the density matrix becoming $2^{15} \times 2^{15}$, which requires a substantial amount of memory and high computational power.

4.5.1 Amplitude-Damping Noise

Amplitude damping describes the phenomenon where a qubit transitions from its excited state $|1\rangle$ to the ground state $|0\rangle$, signifying energy dissipation within the quantum system [32]. This process is also known as the T_1 relaxation [33], [34] and is modeled by the amplitude-damping quantum channel defined by the following Kraus operators:

$$K_0^A = \begin{bmatrix} 1 & 0 \\ 0 & \sqrt{1-\gamma_A} \end{bmatrix}, \quad K_1^A = \begin{bmatrix} 0 & \sqrt{\gamma_A} \\ 0 & 0 \end{bmatrix},$$

where $\gamma_A \in [0, 1]$ is the probability of energy dissipation of the quantum system. This noisy channel leaves the $|0\rangle$ state of the qubit unchanged but changes the state $|1\rangle$ to the state $\sqrt{\gamma_A}|0\rangle + \sqrt{1-\gamma_A}|1\rangle$. Consequently, the quantum state of the image, as defined in Eq. (2), undergoes a transition to a mixed state, as depicted in Eq. (13).

Fig. 11 clearly shows the effect of change in the probability of energy dissipation to the fidelity. It can also be observed from the fidelity diagram that the fidelity decreases as the dissipation probability goes from 0 to 1.

$$\epsilon^A(\rho) = \otimes_{i=0}^9 K_0^{Aq_i} \rho \otimes_{i=0}^9 K_0^{Aq_i \dagger} + \otimes_{i=0}^9 K_1^{Aq_i} \rho \otimes_{i=0}^9 K_1^{Aq_i \dagger}. \quad (13)$$

4.5.2 Phase-Damping Noise

Phase damping refers to the perturbation observed in the off-diagonal elements of the density matrix, leading to a loss in relative phase information within the quantum state [32]. This effect is closely related to the qubit's dephasing time (T_2) [33], [34] and is modeled through phase-damping quantum channels, characterized by Kraus operators:

$$K_0^P = \begin{bmatrix} \sqrt{1-\gamma_P} & 0 \\ 0 & \sqrt{1-\gamma_P} \end{bmatrix}, \quad K_1^P = \begin{bmatrix} \sqrt{\gamma_P} & 0 \\ 0 & 0 \end{bmatrix}, \\ K_2^P = \begin{bmatrix} 0 & 0 \\ 0 & \sqrt{\gamma_P} \end{bmatrix}, \quad (14)$$

where $\gamma_P \in [0, 1]$ represents the probability of losing relative Phase information. The effect of the Phase damping channel on a single qubit state, based on the Kraus operators from Eq. (14), is as follows:

$$|0\rangle \rightarrow (\sqrt{\gamma_P} + \sqrt{1-\gamma_P})|0\rangle, \\ |1\rangle \rightarrow (\sqrt{\gamma_P} + \sqrt{1-\gamma_P})|1\rangle.$$

After passing through this noise channel the original quantum state of the image, as outlined in Eq. (2), transitions into a mixed state represented by Eq. (15). The fidelity F^P of the output state is calculated using Eq. (12). The fidelity variations, corresponding to increasing rates of phase-damping noise, are shown in Fig. 11.

$$\epsilon^P(\rho) = \otimes_{i=0}^{10} K_0^{Pq_i} \rho \otimes_{i=0}^{10} K_0^{Pq_i \dagger} + \otimes_{i=0}^{10} K_1^{Pq_i} \rho \otimes_{i=0}^{10} K_1^{Pq_i \dagger}. \quad (15)$$

4.5.3 Bit-Flip Noise

The bit-flip noisy channel probabilistically flips the state of a quantum bit with a probability parameter $\gamma_B \in [0, 1]$. The Pauli-X gate is known as a bit-flip gate with $\gamma_B = 1$ [32]. This noisy quantum channel is modeled in a quantum circuit using the following Kraus operators:

$$K_0^B = \begin{bmatrix} \sqrt{1-\gamma_B} & 0 \\ 0 & \sqrt{1-\gamma_B} \end{bmatrix}, \quad K_1^B = \begin{bmatrix} 0 & \sqrt{\gamma_B} \\ \sqrt{\gamma_B} & 0 \end{bmatrix}.$$

When the quantum state, as described in Eq. (2), passes through the bit-flip noisy channel, it transforms into a mixed quantum state represented by the density matrix in Eq. (16). Notably, when a single qubit state undergoes this noisy channel, the effects manifest as follows,

$$|0\rangle \rightarrow \sqrt{1-\gamma_B}|0\rangle + \sqrt{\gamma_B}|1\rangle, \\ |1\rangle \rightarrow \sqrt{\gamma_B}|0\rangle + \sqrt{1-\gamma_B}|1\rangle.$$

The fidelity of the resulting noisy quantum state is evaluated using Eq. (12), with Figure 11 illustrating the variation in fidelity across different bit-flip probabilities γ_B ranging from 0 to 1.

$$\epsilon^B(\rho) = \otimes_{i=0}^9 K_0^{Bq_i} \rho \otimes_{i=0}^9 K_0^{Bq_i \dagger} + \otimes_{i=0}^9 K_1^{Bq_i} \rho \otimes_{i=0}^9 K_1^{Bq_i \dagger}. \quad (16)$$

4.5.4 Phase-Flip Noise

In the phase-flip noisy channel, the state of a quantum system is unaffected, but the relative phase of the quantum system flips probabilistically with a parameter $\gamma_W \in [0, 1]$. The Pauli-Z gate is recognized as a phase-flip gate with $\gamma_W = 1$ [32]. This noisy quantum channel is represented in a quantum circuit using the following Kraus operators:

$$K_0^W = \begin{bmatrix} \sqrt{1-\gamma_W} & 0 \\ 0 & \sqrt{1-\gamma_W} \end{bmatrix}, \quad K_1^W = \begin{bmatrix} \sqrt{\gamma_W} & 0 \\ 0 & -\sqrt{\gamma_W} \end{bmatrix}.$$

After transmission through this noisy channel, the quantum state becomes a mixed state, resulting in the loss of phase information from the original state. Specifically, when the quantum state described in Eq. (2) passes through a phase-flip noisy channel, it transforms into Eq. (17). Similarly, the effects on a single qubit state passing through this noisy channel are as follows:

$$|0\rangle \rightarrow (\sqrt{\gamma_W} + \sqrt{1-\gamma_W})|0\rangle, \\ |1\rangle \rightarrow (\sqrt{\gamma_W} + \sqrt{1-\gamma_W})|1\rangle.$$

The fidelity of the Eq. (17) with Eq. (2) is shown in Fig. 11 with all possible values of γ_W from 0 to 1 and is calculated using Eq. (12).

$$\epsilon^W(\rho) = \otimes_{i=0}^9 K_0^{Wq_i} \rho \otimes_{i=0}^9 K_0^{Wq_i \dagger} + \otimes_{i=0}^9 K_1^{Wq_i} \rho \otimes_{i=0}^9 K_1^{Wq_i \dagger}. \quad (17)$$

4.5.5 Bit-Phase-Flip Noise

In the bit-phase-flip noisy channel, a quantum state undergoes concurrent bit-flip and phase-shift operations with a probability $\gamma_F \in [0, 1]$. The Pauli-Y gate is a bit-phase-flip gate with $\gamma_F = 1$ [32]. The Kraus operators to model this noisy channel in a quantum circuit are:

$$K_0^F = \begin{bmatrix} \sqrt{1-\gamma_F} & 0 \\ 0 & \sqrt{1-\gamma_F} \end{bmatrix}, \quad K_1^F = \begin{bmatrix} 0 & -\sqrt{\gamma_F} \\ \sqrt{\gamma_F} & 0 \end{bmatrix}.$$

The mixed state after passing through this noisy channel is written in Eq. (18) and when a single qubit state passes through this noisy channel, the effects are,

$$\begin{aligned} |0\rangle &\rightarrow \sqrt{1-\gamma_F} |0\rangle + \nu\sqrt{\gamma_F} |1\rangle, \\ |1\rangle &\rightarrow -\nu\sqrt{\gamma_F} |0\rangle + \sqrt{1-\gamma_F} |1\rangle. \end{aligned}$$

The variation in the fidelity as per the flipping probability γ_F is shown in Fig. 11, which is calculated by using Eq. (12).

$$\begin{aligned} \epsilon^F(\rho) &= \otimes_{i=0}^9 K_0^{Fq_i} \rho \otimes_{i=0}^9 K_0^{Fq_i\dagger} \\ &+ \otimes_{i=0}^9 K_1^{Fq_i} \rho \otimes_{i=0}^9 K_1^{Fq_i\dagger}. \end{aligned} \quad (18)$$

4.5.6 Depolarization Noise

In Depolarizing noisy environment, the quantum system experiences depolarization with a probability $\gamma_D \in (0, 1)$. This noisy channel applies the Identity, Pauli-X, Pauli-Y, and Pauli-Z operators on the quantum system with probabilities $1 - \gamma_D$, $\gamma_D/3$, $\gamma_D/3$, and $\gamma_D/3$, respectively. The Kraus operators representing this depolarizing noisy channel in a quantum circuit are:

$$\begin{aligned} K_0^D &= \begin{bmatrix} \sqrt{1-\gamma_D} & 0 \\ 0 & \sqrt{1-\gamma_D} \end{bmatrix}, & K_1^D &= \begin{bmatrix} 0 & \sqrt{\frac{\gamma_D}{3}} \\ \sqrt{\frac{\gamma_D}{3}} & 0 \end{bmatrix}, \\ K_2^D &= \begin{bmatrix} 0 & -\nu\sqrt{\frac{\gamma_D}{3}} \\ \nu\sqrt{\frac{\gamma_D}{3}} & 0 \end{bmatrix}, & K_3^D &= \begin{bmatrix} \sqrt{\frac{\gamma_D}{3}} & 0 \\ 0 & \sqrt{\frac{\gamma_D}{3}} \end{bmatrix}. \end{aligned}$$

Upon transmission through this noisy channel, the original quantum state described in Eq. (2) transforms into the mixed state detailed in Eq. (19). For a single qubit state passing through this noisy channel, the effects are as follows:

$$\begin{aligned} |0\rangle &\rightarrow \left(\sqrt{1-\gamma_D} + \sqrt{\frac{\gamma_D}{3}} \right) |0\rangle + (1+\nu)\sqrt{\frac{\gamma_D}{3}} |1\rangle \\ |1\rangle &\rightarrow (1-\nu)\sqrt{\frac{\gamma_D}{3}} |1\rangle + \left(\sqrt{1-\gamma_D} + \sqrt{\frac{\gamma_D}{3}} \right) |1\rangle \end{aligned}$$

The fidelity, calculated using Eq. (12), shows variations as the depolarizing probability γ_D changes, as illustrated in Fig. 11.

$$\begin{aligned} \epsilon^D(\rho) &= \otimes_{i=0}^9 K_0^{Dq_i} \rho \otimes_{i=0}^9 K_0^{Dq_i\dagger} \\ &+ \otimes_{i=0}^9 K_1^{Dq_i} \rho \otimes_{i=0}^9 K_1^{Dq_i\dagger}. \end{aligned} \quad (19)$$

5 CONCLUSION

In this paper, we presented an efficient implementation scheme of a novel enhanced quantum representation (NEQR) for a $2^n \times 2^n$ image, along with quantum image encryption and its decryption procedure on an IBM quantum computer. These algorithms are part of the fittest techniques to represent and encrypt a digital image because of their measurement accuracy and chaotic output with high keyspace and sensitivity. Furthermore, we have shown how to realize each of these procedures on a quantum computer and provided general quantum circuits and algorithms for them. The multi-control-NOT gates are essential to encode the pixel values, whose decomposition into basis one and two-qubit gates increases the circuit complexity as n increases. However, we have provided a method combined with the image compression method to reduce the effect

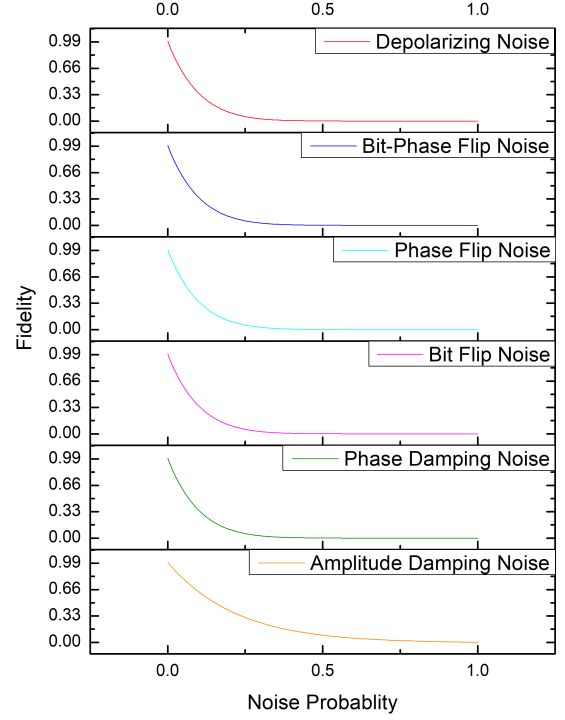


Fig. 11: The plot shows the variation in the fidelity for the quantum state shown in Eq. (2) with the change in noise rate in six different types of noisy channels. Here, the fidelity variation comes out to be similar for all the noisy environments except the Amplitude damping noisy environment.

of decomposition on circuit complexity and successfully reduced it to approximately 50% compared to Zhang et al. for a 2×2 test image on the cost of adding one more qubit to the circuit. Regardless, it is very effective for circuit complexity to make this trade-off between a little extra quantum storage and a significant reduction in circuit complexity. Analysis of the encryption procedure demonstrated that the scheme is sensitive to the encryption key and has enough keyspace to resist ordinary attacks and attacks similar to brute-force attacks. In conclusion, we showed that NEQR, combined with the discussed novel quantum image encryption method, forms a more efficient, secure, feasible, and accurately measurable quantum image processing system. In the future, we would like to demonstrate the implementation of more quantum image representation protocols with an encryption procedure on the quantum computer. This leads to a quantum image processing system with a lower circuit complexity, higher measurement accuracy, and susceptible encryption technique that can be realizable on a quantum computer.

REFERENCES

- [1] R. C. Gonzalez, and R. E. Woods, Digital Image Processing, Publishing House of Electronics Industry, Beijing (2002).
- [2] R. P. Feynman, Simulating physics with computers, Int. J. Theor. Phys., 21(6/7), 467-488 (1982).

- [3] N. Gisin, G. Ribordy, W. Tittel, and H. Zbinden, Quantum cryptography, *Reviews of modern physics*, **74**(1), 145, (2002).
- [4] F. Yan, A. M. Ilyasu, and S. E. Venegas-Andraca, A survey of quantum image representations, *Quantum Inf. Process.*, **15** (2016).
- [5] J. Su, X. Guo, C. Liu and L. Li, A New Trend of Quantum Image Representations, *IEEE Access*, **8** (2020).
- [6] S.E. Venegas-Andraca, and S. Bose, Storing, processing and retrieving an image using quantum mechanics, *Proceeding of the SPIE Conference Quantum Information and Computation*, 137-147 (2003).
- [7] J. I. Latorre, Image compression and entanglement, *arXiv:quant-ph/0510031* (2005).
- [8] S. E. Venegas-Andraca, and J. L. Ball, Processing images in entangled quantum systems, *Quantum Inf. Process.*, **9**(1), 1-11 (2010).
- [9] P. Q. Le, F. Y. Dong, and K. Hirota, A flexible representation of quantum images for polynomial preparation, image compression and processing operations, *Quantum Inf. Process.*, **10**(1), 63-84 (2011).
- [10] B. Sun, A. M. Ilyasu, F. Yan, F. Y. Dong, and K. Hirota, An RGB multi-channel representation for images on quantum computers, *J. Adv. Comput. Intell. Intell. Inf.*, **17**(3), 404-417 (2013).
- [11] Y. Zhang, K. Lu, Y. H. Gao, and M. Wang, NEQR: a novel enhanced quantum representation of digital images, *Quantum Inf. Process.*, **12**(12), 2833-2860 (2013).
- [12] J. Sang, S. Wang, and Q. Li, A novel quantum representation of color digital images, *Quantum Inf. Process.*, **16**(2), 42 (2017).
- [13] H.-S. Li, P. Fan, H.-Y. Xia, H.-L. Peng, and S. X. Song, Quantum implementation circuits of quantum signal representation and type conversion, *IEEE Trans. Circuits Syst. I, Reg. Papers*, vol. **66**, no. 1, 341-354, (2019).
- [14] H. S. Li, Q. X. Zhu, R. G. Zhou, S. Lan, and X. J. Yang, Multi-dimensional color image storage and retrieval for a normal arbitrary quantum superposition state, *Quantum Inf. Process.*, **13**(4), 991-1011 (2014).
- [15] M. Mastriani, Quantum Boolean image denoising, *Quantum Inf. Process.*, **14**(5), 1647-1673 (2014).
- [16] N. Jiang, and L. Wang, Analysis and improvement of the quantum Arnold image scrambling, *Quantum Inf. Process.*, **13**, 1545-1551 (2014).
- [17] Y. G. Yang, X. Jia, S. J. Sun, and Q. X. Pan, Quantum cryptographic algorithm for color images using quantum Fourier transform and double random-phase encoding, *Inf. Sci.*, **277**, 445-457 (2014).
- [18] H.-R. Liang, X.-Y. Tao, and N.-R. Zhou, Quantum image encryption based on generalized affine transform and logistic map, *Quantum Inf. Process.*, **15**(7), 2701-2724 (2016).
- [19] Q. W. Ran, L. Wang, J. Ma, *et al.*, A quantum color image encryption scheme based on coupled hyper-chaotic Lorenz system with three impulse injections, *Quantum Inf. Process.*, **17**, 188 (2018).
- [20] N. R. Zhou, W. W. Chen, X. Y. Yan, and Y. Q. Wang, Bit-level quantum color image encryption scheme with quantum cross-exchange operation and hyper-chaotic system, *Quantum Inf. Process.*, **17**, 137 (2018).
- [21] R. L. Devaney, *An Introduction to Chaotic Dynamical Systems*, Westview Press, Boulder (2003).
- [22] R. K. Brayton, A. Sangiovanni-Vincentelli, C. McMullen, and G. Hachtel: *Log. Minimization Algorithms VLSI Synth*, Kluwer Academic Publishers, Dordrecht (1984).
- [23] K. H. Rosen, *Elementary Number Theory and Its Applications*, United Kingdom, Pearson/Addison Wesley (2005).
- [24] N. Jiang, and L. Wang, Analysis and improvement of the quantum Arnold image scrambling, *Quantum Inf. Process.*, **13**(7), 1545-1551 (2014).
- [25] Qiskit: An Open-source Framework for Quantum Computing, (2019). [10.5281/ZENODO.2562111](https://zenodo.org/record/2562111)
- [26] S. Miyake and K. Nakamae, A quantum watermarking scheme using simple and small-scale quantum circuits, *Quantum Information Processing* **15**, 1849-1864 (2016).
- [27] M. Naseri, H. Shahrokh, M. Baghfalaki, R. Gheibi, J. Batle, A. Farouk, and A. Habibi, A new secure quantum watermarking scheme, *Optik* **139**, 77-86 (2017).
- [28] Z. Wang, and H. R. Sheikh, Image Quality Assessment: From Error Visibility to Structural Similarity, *IEEE Transactions on Image Processing*, **13**, No. 4 (2004).
- [29] U. Sara, M. Akter, and M. Uddin, Image Quality Assessment through FSIM, SSIM, MSE and PSNR—A Comparative Study, *Journal of Computer and Communications*, **7**, 8-18 (2019).
- [30] R. G. Deshpande, L. L. Ragha, and S. K. Sharma, Video Quality Assessment through PSNR Estimation for Different Compression Standards, *Indonesian Journal of Electrical Engineering and Computer Science*, **11**, 918-924 (2018).
- [31] K. Kraus, *States, Effects and Operations*, Springer-Verlag, Berlin, (1983).
- [32] M. Nielsen, and I. Chuang, *Quantum Computation and Quantum Information: 10th Anniversary Edition*. Cambridge: Cambridge University Press (2010).
- [33] N. P. Sawaya, M. Smelyanskiy, J. R. McClean, and A. Aspuru-Guzik, Error sensitivity to environmental noise in quantum circuits for chemical state preparation, *Journal of chemical theory and computation* **12**, 3097 (2016).
- [34] B. Rost, B. Jones, M. Vyushkova, A. Ali, C. Cullip, A. Vyushkov, and J. Nabrzycki, Simulation of thermal relaxation in spin chemistry systems on a quantum computer using inherent qubit decoherence (2020).